3-5 μm Mid-Infrared Broadband Perfect Absorber Based on Ti Ring Embedded Structure

Yun Fang, *Member, IEEE*, Li Gong, Sixuan Huang, Shuzhan Yan, and Xue Zhang, *Member, IEEE*

***Abstract*—In this work, a 3-5 μm mid-infrared broadband perfect absorber is proposed. The proposed absorber is only composed of an aluminium oxide (Al_2O_3) dielectric layer on the top, a silicon (Si) dielectric layer with an embedded titanium (Ti) ring in the middle and a high loss metal substrate. It exhibits an extremely perfect absorption performance in the entire range of 3-5 μm mid-infrared band, with the highest and average absorption rates of 99.91% and 98.57%, respectively. The excellent absorption at 3-5 μm is attributed to the intrinsic absorption of the two dielectrics and the excitation of the surface plasmon resonance (SPR). Moreover, the average absorption rate can be still maintained above 91.33% when the incident angle of TE/TM or unpolarized wave reaches 60°, and there is almost unchanged in the absorption rate when the polarization angle of the incident wave gradually changes from 0° to 90°, which shows the insensitivity of the absorber to the incident and polarization angle. The absorber with simple structure and high stability has potential application prospects in infrared stealth and detection.**

***Index Terms*—Mid-infrared, embedded, perfect absorber, broadband, surface plasmon resonance (SPR).**

I. Introduction

BROADBAND absorbers play a significant role in various fields, including electromagnetic stealth [1], thermal capture [2], photoelectric detection [3], [4], [5], [6], imaging [7], [8], [9], sensing [10], [11]. The utilization of high-loss metals in place of conventional noble metals for designing metamaterial structures is a prevalent approach to achieve broadband absorption [12], [13], [14], [15], [16], [17]. For example, Feng et al. proposed a metal-dielectric metamaterial absorber based on the high-loss metal titanium (Ti) to achieve broadband absorption in the violet infrared to near infrared [12]. Luo et al. presented a tungsten-based metamaterial absorber to achieve high coherent absorption at 1.32-3.28 μm [16]. Another way to achieve broadband absorption is through the stacking of resonators with different sizes in the vertical direction [18], [19], [20]. For instance, Li et al. designed a trapezoidal multilayer grating array structure with optical absorption at 3.5-4.8 μm, which resulted in a thicker absorber structure and thereby increasing the difficulty of processing [18]. Subsequently, a square double-layer grating array was demonstrated to achieve an average absorption of 98.3% at 0.3-2.1 μm. This design reduced the number of stacked layers while improving the overall absorption performance of the structure [20]. Broadband absorption can also be achieved by placing multiple resonators of different frequencies in the horizontal direction [21], [22]. For instance, Qin et al. employed a metal-dielectric-metal sandwich composite structure with resonant units of various sizes to attain three-peak broadband absorption in the long-wave infrared [22].

In general, an increase in bandwidth inevitably leads to a decrease in the absorption capacity of an absorber. Consequently, a variety of approaches have been proposed to enhance light absorption. One such approach is to employ a microcavity structure, which enables light to pass through the absorption layer multiple times, thereby enhancing absorption [23], [24]. The second one is to make full use of external stimuli such as adding bias voltage to modify the absorption capacity of the structure [25], [26], [27]. This method is typically used for materials that are sensitive to polarization voltage, such as graphene and vanadium dioxide. The third one is to manually manipulate plasma resonance by adjusting structural features [28], [29], [30], [31].

The aforementioned absorbers mainly involve bands in the microwave, THz, long-wave infrared (LWIR), and visible-near-infrared bands, rarely mentioning the 3-5 μm band alone. Achieving broadband perfect absorption in specific bands simultaneously is challenging. However, it is well known that the 3-5 μm spectral region is both an atmospheric window and a molecular fingerprint region, and absorbers covering this band are not affected by bad weather in infrared imaging application. Therefore, the further study of the 3-5 μm band absorbers is of great significance. Recently, Hou et al. proposed a composite cross structure that achieved 98.2% absorption at 4.28 μm, but its absorption bandwidth was relatively narrow [32]. In the same year, Cao et al. achieved over 81% integrated absorption in the 2.5-6 μm spectral range and over 96% average absorption in the 3-5 μm range by designing different sized cavities. However, this structure was complex and difficult to process [33]. Subsequently, Li et al. utilized oblique angle deposition technology to prepare a layered nanorod array structure with different tilt angles, achieving broadband absorption of 82.9% in the 3-5 μm range, but the absorption rate was not very high [34].

Manuscript received 31 July 2023; accepted 2 August 2023. Date of publication 7 August 2023; date of current version 14 August 2023. This work was supported in part by the National Natural Science Foundation of China under Grants 62201489 and 62101476, in part by the Natural Science Foundation of Hunan Province of China under Grant 2022JJ40450, and in part by the Scientific Research Program through the Hunan Provincial Education Department under Grant 20C1772. *(Corresponding author: Xue Zhang.)*

The authors are with the School of Automation and Electronic Information, Xiangtan University, Xiangtan 411105, China (e-mail: fangyun@xtu.edu.cn; 15525664288@163.com; 15273053919@163.com; szyan19990712@163.com; zhangxue.iecas@yahoo.com).

Digital Object Identifier 10.1109/JPHOT.2023.3302276

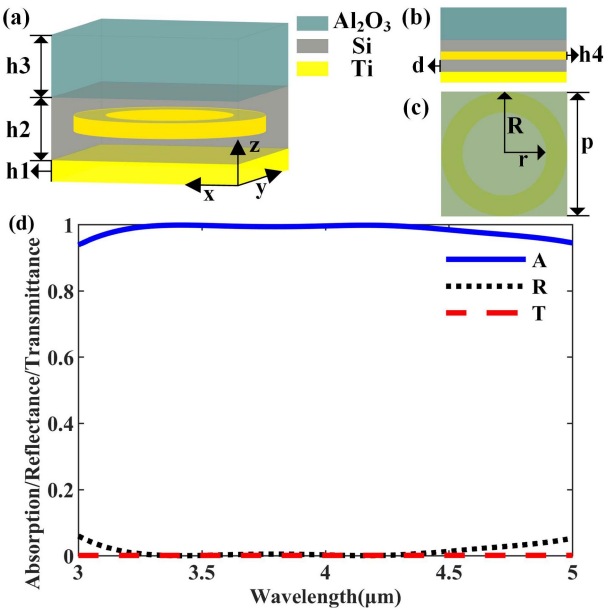

Fig. 1. The schematic diagram of the proposed absorber. (a) Three-dimensional schematic of a unit cell of the absorber. (b) Front view of the unit cell. (c) Top view of the unit cell. (d) Spectrogram of the absorber.

In this paper, we propose a 3-5 μm mid-infrared broadband perfect absorber, which is only composed of an aluminium oxide (Al_2O_3) dielectric layer on the top, a Si dielectric layer with an embedded Ti ring in the middle, and a Ti metal plate at the bottom. Numerical results show an extremely perfect absorption performance in the entire range of 3-5 μm mid-infrared band with the highest and average absorption rates of 99.91% and 98.57%, respectively. Furthermore, the absorption mechanism of the proposed absorber is investigated by analyzing the electric and magnetic fields in the absorption bands. Subsequently, we also examined the variation of the absorption rate with the structure parameters, which affect the position of the absorption peaks as well as the overall absorption rate. Finally, we investigated the effect of the incident and polarization angle of the light source on the absorption rate, and found that the absorber is insensitive to incident and polarization angle. This absorber has a simple structure and high stability, making it a promising candidate for infrared stealth and detection applications.

II. Structure Design and Simulation Model

The three-dimensional schematic of a unit cell of the mid-infrared broadband perfect absorber is demonstrated in Fig. 1(a). It is composed of an Al_2O_3 dielectric layer on the top, a silicon (Si) dielectric layer of embedded Ti ring in the middle, and a high loss metal Ti substrate at the bottom. The structure is symmetric along the x and y directions, which indicates the polarization-independent optical response of the proposed absorber. The Al_2O_3 on the top acts as an anti-reflective protective layer, the Si dielectric layer with an embedded Ti ring in the middle plays the role of inducing resonance and also effectively preventing the oxidation of metal Ti, and the metal Ti substrate acts as reflector for blocking the transmitted wave. Fig. 1(b) and (c) present the front and top views of the unit cell, respectively. The absorber is a periodic array in the x and y directions, and the period is expressed by p. The thickness of the metal substrate, the Si, the Al_2O_3 and the ring are expressed as h1, h2, h3 and h4, respectively. The inner and outer radii of the ring are expressed as r and R respectively, and the distance between the ring and the substrate is expressed as d. Using the optimized design, the geometric parameters are as follows: h2 = 0.6 μm, h3 = 0.6 μm, h4 = 0.15 μm, r = 0.6 μm, R = 0.9 μm, d = 0.175 μm, and p = 1.8 μm. Further, the thickness of the bottom Ti substrate (h1) is set at 0.2 μm to ensure zero transmission. The proposed structure can be fabricated using the following steps: (1) deposition of Si and photoresist (PR) films on Ti substrate; (2) formation of circular trench by using e-beam lithography; (3) deposition of Ti ring, followed by lifting off the PR; (4) deposition of Si layer and Al_2O_3 layer.

Numerical simulations are performed using the finite-difference time-domain (FDTD) method to calculate the electromagnetic response and electromagnetic field distribution, with the incident light wavelength set to 3-5 μm. The periodic boundary conditions are employed in the x and y directions, and the perfectly matched layer (PML) boundary conditions are applied in the z direction to truncate the electromagnetic wave. The unpolarized plane wave is vertically incident from the top of the structure along the negative z-axis. Meanwhile, two monitors are placed beneath the substrate and on the back of the light source to monitor the transmittance T and reflectance R of the structure, respectively. Thus, the absorption A can be calculated using the formula: A = 1-T-R. The optical parameters of both Si and Al_2O_3 materials are taken from the data of Palik [35] and the dielectric constant of Ti can be described by the Drude Lorenz model [36] and is expressed as:

$$\varepsilon = 1 - \frac{\Omega_p^2}{\omega(\omega - i\Gamma_0)} + \sum_{j=1}^{k} \frac{f_j \omega_p^2}{(\omega_j^2 - \omega^2 + i\omega\Gamma_j)} \quad (1)$$

where $\Omega_p = \sqrt{f_0}\omega_p$ is the plasma frequency associated with intraband transitions with oscillator strength f_0 and damping constant Γ_0, ω_p is the plasma frequency with a value of 7.29 eV, $1/\Gamma_j$ is lifetime, k is the number of oscillators.

The absorption, reflectance, and transmittance spectrum of the absorber are calculated by simulations, as shown in Fig. 1(d). As depicted by the red and black dashed lines, both transmittance and reflectance are close to zero. Therefore, the absorption rate of the proposed absorber is extremely high in the 3-5 μm range according to A = 1-R-T, as shown in the Fig. 1(d). It can also be observed that the absorption peak is not obvious in the 3-5 μm band. With the help of simulation tools, the frequency positions of the two absorption peaks are obtained, which are at 3.41 μm and 4.16 μm, and the corresponding absorption rates are 99.91% and 99.88%, respectively. Due to higher absorption across the 3-5 μm spectrum, resulting in the average absorption rate as high as 98.57%, achieving perfect absorption.

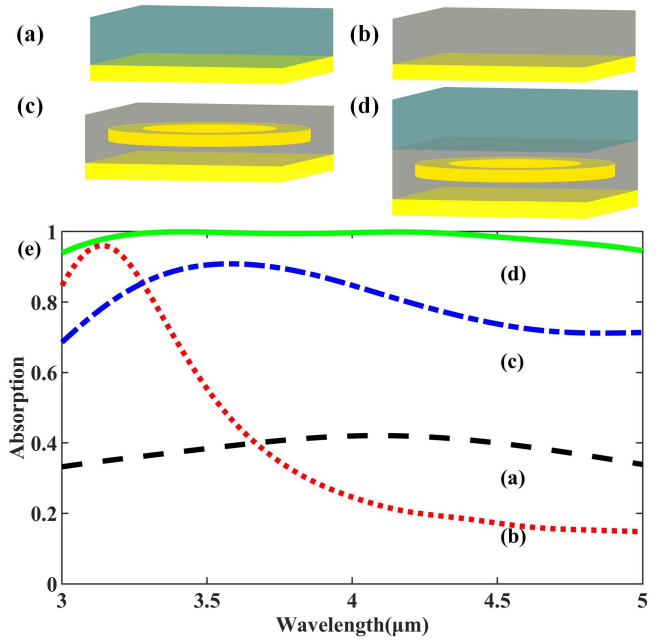

Fig. 2. (a) Substrate Ti and Al_2O_3 structure. (b) Substrate Ti and Si structure. (c) Substrate Ti and Si with an embedded Ti ring structure. (d) Complete structure. (e) Absorption spectrum of decomposed structure.

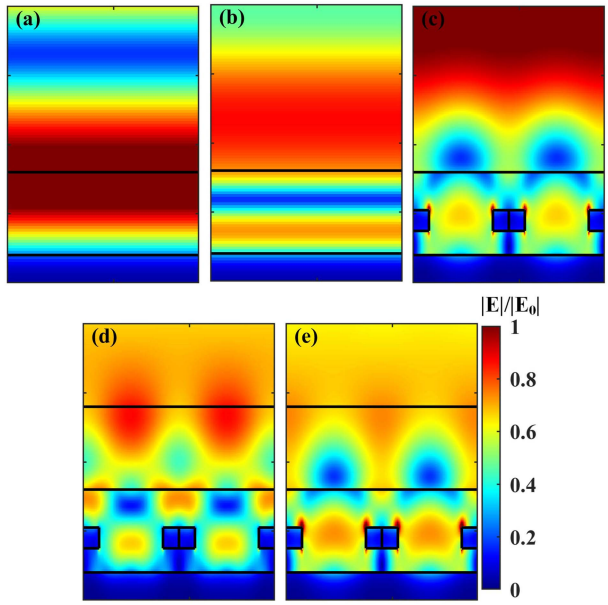

Fig. 3. Electric field distribution at the (a) peak of substrate Ti and Al_2O_3 structure, (b) peak of substrate Ti and Si structure, (c) peak of substrate Ti and Si with an embedded Ti ring structure, (d) 3.41 μm peak of the complete structure, (e) 4.16 μm peak of the complete structure.

III. Results and Discussions

A. Mechanism for Broadband Perfect Absorption

To gain insights into the absorption mechanism of the proposed absorption structure, we first decomposed it into different kinds of simple structure and compared their absorption spectra, as shown in Fig. 2. Fig. 2(a) illustrates the absorption structure consisting of an Al_2O_3 dielectric layer on top of a Ti substrate, whose absorption spectrum corresponds to the curve (a) in Fig. 2(e). It is shown that the absorption rate of the structure is not high across the entire 3-5 μm band. Fig. 2(b) represents the combination of substrate Ti and dielectric Si, and its absorption spectrum is the curve (b) in Fig. 2(e). It is observed that spectral absorption is greater than 80% in the initial wavelength, but abruptly decreases to less than 20% at higher wavelength. This structure has a higher absorption in a narrow bandwidth compared to the first absorption structure, indicating that Si in the structure induces resonance. Fig. 2(c) displays that a Ti ring is embedded into the Si dielectric layer based on structure (b), and the absorption spectrum corresponds to the curve (c) in Fig. 2(e). It can be clearly seen that the absorption bandwidth is broadened, indicating that the embedding of the Ti ring plays a crucial role in broadening the absorption spectrum. Fig. 2(d) indicates that the complete absorption unit cell is achieved by adding an Al_2O_3 anti-reflective protective layer on top of the structure based on (c) structure, and the absorption spectrum corresponds to the curve (d) in Fig. 2(e). It is evident that the absorption of the proposed absorption structure enhances by approximately 16% to achieve perfect absorption due to the utilization of Al_2O_3 anti-reflective protective layer compared to the structure (c).

Thereafter, we selected two structural units from the decomposed structure and investigated their electric and magnetic field distributions in the x-z cross section at the absorption peak. Fig. 3(a) and (b) display the electric field distributions at the absorption peak of the structure in Fig. 2(a) and (b). Although the location and intensity of the electric field distribution differ between the two structures, the electric field intensity is uniformly distributed in the horizontal direction in both cases, indicating that the main factor causing absorption in both structures is the intrinsic absorption of the material [37], [38]. Fig. 4(a) and (b) show the magnetic field distribution at the absorption peaks of the structures in Figs. 2(a) and (b). Once again, the magnetic field distribution confirms that the absorption of the structures is due to the presence of intrinsic absorption of the material. Fig. 3(c) shows the electric field distribution at the absorption peak of the structure in Fig. 2(c). The embedding of the Ti ring causes a significant change in the electric field distribution compared to the electric field distribution in Fig. 3(b), when the electric field is mainly concentrated in the air above the structure. Fig. 4(c) illustrates the magnetic field distribution of the structure in Fig. 2(c), displaying a significant magnetic field enhancement on the surface of the Ti ring and in the dielectric layer below the Ti ring. This enhancement is due to the high loss characteristics of Ti, which results in a large resonance Q-factor [12], [39]. This means that surface plasmon resonance (SPR) [40], [41], [42], [43] is excited in the material, leading to a magnetic field coupled with the dielectric. The electric field distributions at the two absorption peaks of the complete structure are shown in Fig. 3(d) and (e). It is apparent that the addition of Al_2O_3 causes the electric field in the air to be pulled back into the structure, indicating the crucial role of the Al_2O_3 layer in preventing the

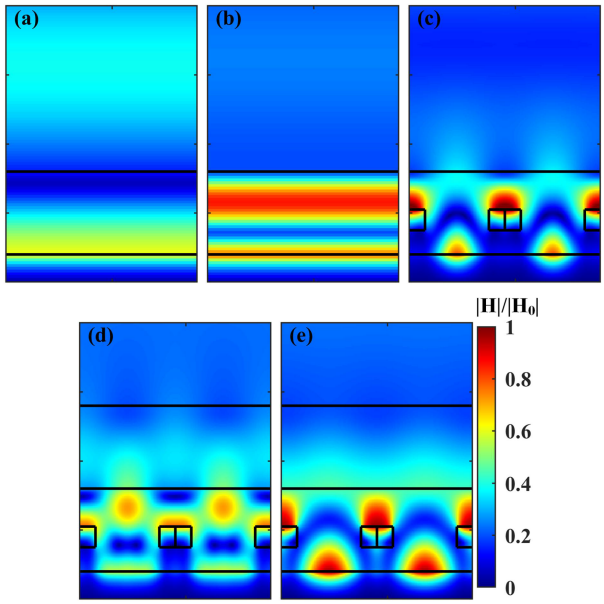

Fig. 4. Magnetic field distribution at the (a) peak of substrate Ti and Al_2O_3 structure, (b) peak of substrate Ti and Si structure, (c) peak of substrate Ti and Si with an embedded Ti ring structure, (d) 3.41 μm peak of the complete structure, (e) 4.16 μm peak of the complete structure.

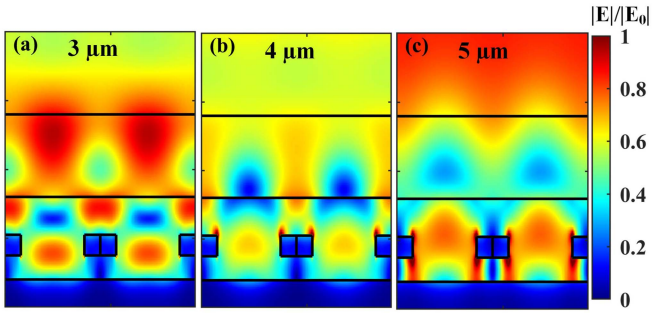

Fig. 5. Electric field distribution of the complete structure at the (a) 3 μm, (b) 4 μm, (c) 5 μm.

electric field from reflecting back into the air. Fig. 4(d) and (e) depict the magnetic field distributions at the absorption peaks at 3.41 μm and 4.16 μm of the structure in Fig. 2(d). It is worth noting that the magnetic field distributions at the two locations are not identical, suggesting that the main mechanisms causing the absorption at the two locations are distinct, with the absorption at 3.41 μm dominated by the resonance of the structure and the absorption at 4.16 μm dominated by the SPR. Thus, the perfect absorption of the absorber can be attributed to the coupling of multiple resonances.

To further investigate the absorption mechanism and distribution of absorption bands, we took two units and analyzed the electric and magnetic field distributions of the x-z cross section at three different wavelengths of 3 μm, 4 μm and 5 μm, respectively. As shown in Fig. 5, the electric field of the 3 μm incident wave is primarily distributed in the Al_2O_3 dielectric, whereas the maximum electric field intensity of the 4 μm incident wave

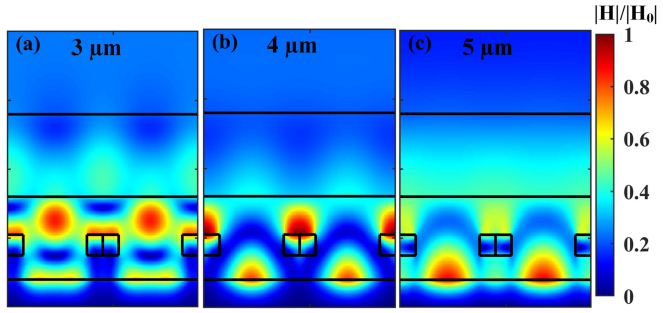

Fig. 6. Magnetic field distribution of the complete structure at the (a) 3 μm, (b) 4 μm, (c) 5 μm.

is distributed in the upper inner edge of Ti ring, and the electric field of the 5 μm incident wave is concentrated at the inner side of the Ti ring structure and at the center of the ring. This indicates that as the length of the incident wave increases, the position of the electric field penetrates deeper into the absorption structure. Similarly, the magnetic field distribution in Fig. 6 also shows that the magnetic field deepens into the structure with increasing incident wavelength. This is because the resonance gradually slows down and the resulting resonance wavelength also gradually becomes longer [18].

B. *The Effect of Structural Parameters on Absorption*

We also analyzed the optimization process of the six variable structural parameters in the complete structure. Fig. 7 illustrates that geometric parameters have a significant impact on its absorption performance. When discussing a change in any of the following parameters, the other parameters remain unchanged. As shown in Fig. 7(a), when the thickness of Al_2O_3 gradually increases, the absorption peak has an obvious red shift. This is because the increase in dielectric layer thickness leads to a change in the equivalent impedance of the resonant top layer relative to the free space [44]. In Fig. 7(b), the change in dielectric Si thickness only affects the absorption rate of the 3-4 μm band, since the intrinsic absorption and SPR of Si occur in this band. In Fig. 7(c)–(f), the influence of ring height, thickness, inner radius, and outer radius on the absorption rate is respectively represented. As depicted in Fig. 7(c), as the ring height increases from 0.275 μm to 0.45 μm, the absorption rate of the entire band gradually increases. However, as the ring height continues to increase, the absorption rate decreases, and the change in absorption curve becomes more drastic. This is because SPR occurs on the ring surface, and changing the height of the ring directly affects the shape and strength of the SPR, thus affecting the absorption rate. As shown in Fig. 7(d), the thickness of the ring also affects the absorption rate, and the position of the absorption peak changes with the thickness of the ring. It can be seen from Fig. 7(e) and (f) that the change in inner radius of the Ti ring has a small impact on the overall absorption rate, while the change of outer radius has a significant impact on the absorption rate, with a larger outer radius resulting in better absorption performance.

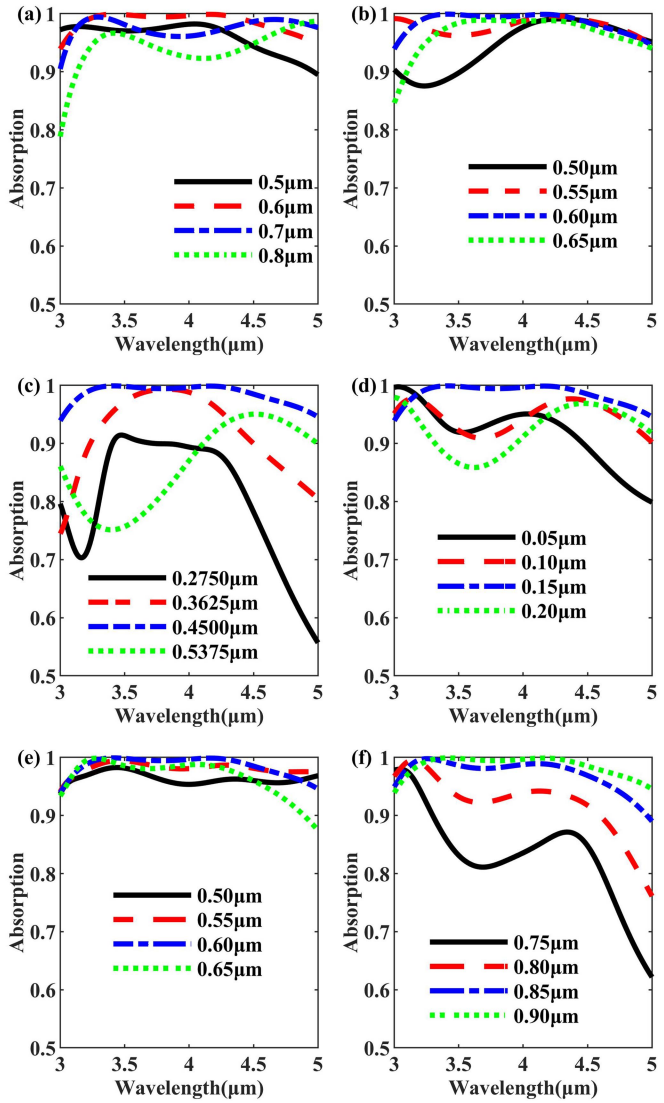

Fig. 7. Influence of (a) Al_2O_3 thickness on absorption properties, (b) Si thickness on absorption properties, (c) ring height on absorption properties, (d) ring thickness on absorption properties, (e) inner radius of ring on absorption properties, (f) outer radius of ring on absorption properties.

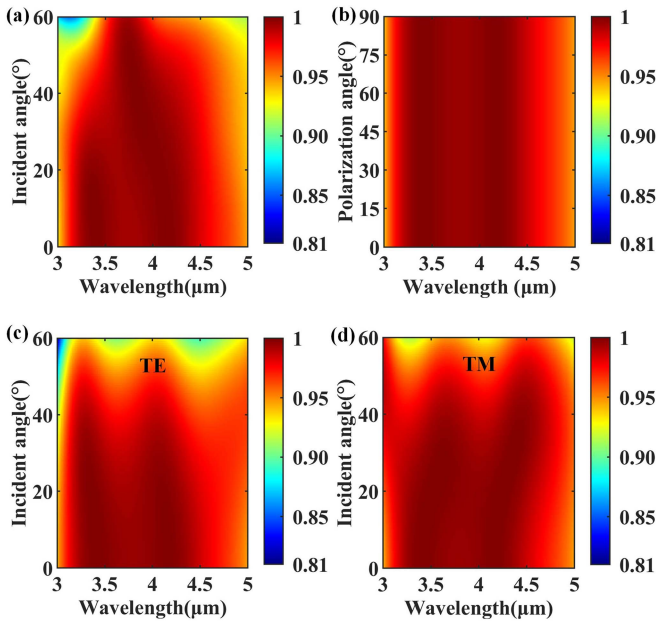

Fig. 8. The dependence of the absorption features of the proposed absorber on the (a) unpolarized wave incident angle, (b) polarization angle, (c) TE wave incident angle, (d) TM wave incident angle.

C. *Effects of Different Incident and Polarization Angles on Absorption*

In practical electromagnetic environments, absorbers are often required to absorb incoming signals from different directions when integrated with detectors. Therefore, the influence of the different incident and polarization angles on the absorption of the structure should also be analyzed. Fig. 8(a) shows the dependence of the absorption features of the proposed absorber on the unpolarized wave incident angle. As shown, a slight change occurs in the two absorption peaks when the incident angle ranges from 0° to 30°, and as the incident angle increases, the left peak gradually disappears and fuses with the right peak to form an absorption peak. The fusion absorption peak has a blue shift relative to the right peak, which is due to the hybridization of the two absorption peaks [45], [46]. However, even when the incidence angle is 60°, the average absorption rate for the entire 3-5 μm band is still above 93.55%, indicating that the structure is insensitive to the unpolarized wave incident angle. Fig. 8(b) represents the effect of the polarization angle on the absorption rate, from which we can see that the absorption rate is almost unchanged, and the average absorption is still 98.57% when the polarization angle reaches 90°, which indicates the polarization insensitivity of the present structure. Fig. 8(c) and (d) represent the effects on the absorption rate for different incident angles of TE and TM waves, respectively, and we can see that the two absorption peaks have different degrees of deviation, but the average absorption is still as high as 91.33% and 94.03% when the incident angles of TE and TM waves reach 60°, which indicates that the structure is insensitive to the incident angle of TE and TM waves.

IV. Conclusion

In conclusion, we propose an embedded broadband perfect absorber that covers the entire 3-5 μm mid-infrared band with the highest and average absorption rates of 99.91% and 98.57%, respectively. It is only composed of an Al_2O_3 dielectric layer on the top, a Si dielectric layer with an embedded Ti ring in the middle and a high loss metal substrate. Firstly, the absorption mechanism of the proposed absorber is investigated by analyzing the electric and magnetic fields in the absorption bands, confirming the generation of SPR and the intrinsic absorption of the material. Next, the influence of the geometrical parameters of the absorber structure on its absorption performance is analyzed. Finally, we investigated the effect of the incident and polarization angle of the light source on the absorption rate, and found that the absorber is insensitive to incident and polarization angle. Such an absorber with simple structure and high stability has potential application prospects in infrared stealth and detection.

REFERENCES

[1] C. Yang et al., "Thermal infrared and broadband microwave stealth glass windows based on multi-band optimization," *Opt. Exp.*, vol. 29, no. 9, pp. 13610–13623, Apr. 2021.

[2] M. Desouky, A. M. Mahmoud, and M. A. Swillam, "Silicon based mid-IR super absorber using hyperbolic metamaterial," *Sci. Rep.*, vol. 8, Feb. 2018, Art. no. 2036.

[3] S. Ogawa, S. Fukushima, and M. Shimatani, "Hexagonal-boron nitride/graphene van der Waals heterostructure-based wavelength-selective infrared absorbers using plasmonic metasurfaces for multi-spectral infrared photodetectors," *J. Opt. Soc. Amer. B*, vol. 39, no. 12, pp. 3149–3158, Dec. 2022.

[4] M. Vallone et al., "Plasmon-enhanced light absorption in mid-wavelength infrared HgCdTe detectors," *IEEE J. Sel. Topics Quantum Electron.*, vol. 28, no. 2, Mar./Apr. 2022, Art. no. 3802310.

[5] J. Zhao and Y. Cheng, "Temperature-tunable terahertz perfect absorber based on all-dielectric strontium titanate (STO) resonator structure," *Adv. Theory Simul.*, vol. 5, no. 12, May 2022, Art. no. 2200520.

[6] Y. Cheng and J. Zhao, "Simple design of a six-band terahertz perfect metasurface absorber based on a single resonator structure," *Physica Scripta*, vol. 97, no. 9, Aug. 2022, Art. no. 095508.

[7] S. Jiang, J. Li, J. Li, J. Lai, and F. Yi, "Metamaterial microbolometers for multi-spectral infrared polarization imaging," *Opt. Exp.*, vol. 30, no. 6, pp. 9065–9087, Mar. 2022.

[8] Y. Bai et al., "Ultrafast chemical imaging by widefield photothermal sensing of infrared absorption," *Sci. Adv.*, vol. 5, no. 7, Jul. 2019, Art. no. eaav7127.

[9] J. Li et al., "Inverse design of multifunctional plasmonic metamaterial absorbers for infrared polarimetric imaging," *Opt. Exp.*, vol. 27, no. 6, pp. 8375–8386, Mar. 2019.

[10] A. Livingood et al., "Filterless nondispersive infrared sensing using narrowband infrared emitting metamaterials," *Amer. Chem. Soc. Photon.*, vol. 8, no. 2, pp. 472–480, Jan. 2021.

[11] Y. Cheng, Y. Qian, H. Luo, F. Chen, and Z. Chen, "Terahertz narrowband perfect metasurface absorber based on micro-ring-shaped GaAs array for enhanced refractive index sensing," *Physica E: Low Dimens. Syst. Nanostructures*, vol. 146, Jan. 2023, Art. no. 115527.

[12] H. Feng et al., "Ultrabroadband metamaterial absorbers from ultraviolet to near-infrared based on multiple resonances for harvesting solar energy," *Opt. Exp.*, vol. 29, no. 4, pp. 6000–6010, Feb. 2021.

[13] H. Feng et al., "Tunable polarization-independent and angle-insensitive broadband terahertz absorber with graphene metamaterials," *Opt. Exp.*, vol. 29, no. 5, pp. 7158–7167, Mar. 2021.

[14] Z. Qin et al., "Broadband long-wave infrared metamaterial absorber based on single-sized cut-wire resonators," *Opt. Exp.*, vol. 29, no. 13, pp. 20275–20285, Jun. 2021.

[15] F. Li et al., "Polarization-dependent wideband metamaterial absorber for ultraviolet to near-infrared spectral range applications," *Opt. Exp.*, vol. 30, no. 15, pp. 25974–25984, Jul. 2022.

[16] P. Luo, G. Lan, J. Nong, X. Zhang, T. Xu, and W. Wei, "Broadband coherent perfect absorption employing an inverse-designed metasurface via genetic algorithm," *Opt. Exp.*, vol. 30, no. 19, pp. 34429–34440, Sep. 2022.

[17] M. A. Baqir, "Wide-band and wide-angle, visible- and near-infrared metamaterial-based absorber made of nanoholed tungsten thin film," *Opt. Mater. Exp.*, vol. 9, no. 5, pp. 2358–2367, May 2019.

[18] Y. Li, L. Li, F. Wang, H. Ge, R. Xie, and B. An, "Two broad absorption bands in infrared atmosphere transparent windows by trapezoid multilayered grating," *Opt. Mater. Exp.*, vol. 10, no. 2, pp. 682–692, Feb. 2020.

[19] S. Mehrabi, R. M. H. Bilal, M. A. Naveed, and M. M. Ali, "Ultra-broadband nanostructured metamaterial absorber based on stacked square-layers of TiN/TiO2," *Opt. Mater. Exp.*, vol. 12, no. 6, pp. 2199–2211, Jun. 2022.

[20] H. Cai, Y. Sun, X. Wang, and S. Zhan, "Design of an ultra-broadband near-perfect bilayer grating metamaterial absorber based on genetic algorithm," *Opt. Exp.*, vol. 28, no. 10, pp. 15347–15359, May 2020.

[21] H. Yu et al., "Polarization-dependent broadband absorber based on composite metamaterials in the long-wavelength infrared range," *Opt. Exp.*, vol. 29, no. 22, pp. 36111–36120, Oct. 2021.

[22] Z. Qin et al., "Multi-mode plasmonic resonance broadband LWIR metamaterial absorber based on lossy metal ring," *Opt. Exp.*, vol. 30, no. 1, pp. 473–483, Jan. 2022.

[23] T. Yoshinaga, K. Hashimoto, N. Teranishi, and A. Ono, "Photon confinement in a silicon cavity of an image sensor by plasmonic diffraction for near-infrared absorption enhancement," *Opt. Exp.*, vol. 30, no. 20, pp. 35516–35525, Sep. 2022.

[24] N. Nguyen-Huu et al., "Ultra-wide spectral bandwidth and enhanced absorption in a metallic compound grating covered by graphene monolayer," *IEEE J. Sel. Topics Quantum Electron.*, vol. 27, no. 1, Jan./Feb. 2021, Art. no. 8500108.

[25] G. Liu et al., "High-performance electro-optic manipulation by plasmonic light absorber with nano-cavity field confinement," *IEEE Photon. J.*, vol. 13, no. 3, pp. 1–9, Jun. 2021.

[26] L. Wang et al., "Improving light extraction efficiency of AlGaN-based deep ultraviolet light-emitting diodes by combining thinning p-AlGaN/p-GaN layer with Ni/Au/Al high-reflectivity electrodes," *IEEE Photon. J.*, vol. 15, no. 2, Apr. 2023, Art. no. 8200305.

[27] Z. Yan et al., "Ultra-broadband and completely modulated absorption enhancement of monolayer graphene in a near-infrared region," *Opt. Exp.*, vol. 30, no. 19, pp. 34787–34796, Sep. 2022.

[28] J. Huang, J. Li, D. Liu, L. Miao, and C. Zhao, "Enhancement of optical nonlinearity in the triangular gold nanoplates on indium tin oxide," *IEEE Photon. J.*, vol. 13, no. 3, Jun. 2021, Art. no. 3000208.

[29] S. El-Jallal et al., "Photonic crystal backbone for light trapping inside an ultrathin, low absorbing layer," *Opt. Exp.*, vol. 30, no. 16, pp. 29694–29707, Aug. 2022.

[30] C. Hu et al., "Plasmonic nano-focusing enhancement of nano-rhombus-shaped resonators in the sub-diffraction limit for highly efficient light-wave collection," *Opt. Mater. Exp.*, vol. 12, no. 8, pp. 3313–3326, Aug. 2022.

[31] B. Tang, N. Yang, L. Huang, J. Su, and C. Jiang, "Tunable anisotropic perfect enhancement absorption in black phosphorus-based metasurfaces," *IEEE Photon. J.*, vol. 12, no. 3, Jun. 2020, Art. no. 4500209.

[32] E. Hou et al., "Dual-band metamaterial absorber with a low-coherence composite cross structure in mid-wave and long-wave infrared bands," *Opt. Exp.*, vol. 29, no. 22, pp. 36145–36154, Oct. 2021.

[33] B. Cao, C. Li, W. Shi, C. Han, Y. Wu, and C. Yan, "Large-area mid-infrared broadband absorbers based on spiral ITO resulting from the combination of two different broadening absorption methods," *Opt. Exp.*, vol. 29, no. 21, pp. 34427–34440, Oct. 2021.

[34] L. Li et al., "3-5 μm mid-infrared broadband absorbers composed of layered ITO nanorod arrays with high visible light transmittance," *Opt. Exp.*, vol. 30, no. 13, pp. 23840–23851, Jun. 2022.

[35] E. D. Palik, *Handbook of Optical Constants of Solids*. New York, NY, USA: Academic, 1998.

[36] A. D. Rakić, A. B. Djurišić, J. M. Elazar, and M. L. Majewski, "Optical properties of metallic films for vertical-cavity optoelectronic devices," *Appl. Opt.*, vol. 37, no. 22, pp. 5271–5283, Aug. 1998.

[37] H. Zhou, Q. Sang, X. Wang, and X. Chen, "Symmetrical metal cladding waveguide for absorption sensing and its sensitivity analysis," *IEEE Photon. J.*, vol. 9, no. 1, Feb. 2017, Art. no. 6800509.

[38] J. M. Elson and C. C. Sung, "Intrinsic and roughness-induced absorption of electromagnetic radiation incident on optical surfaces," *Appl. Opt.*, vol. 21, no. 8, pp. 1496–1501, Apr. 1982.

[39] Z. Li, Y. Cheng, H. Luo, F. Chen, and X. Li, "Dual-band tunable terahertz perfect absorber based on all-dielectric InSb resonator structure for sensing application," *J. Alloys Compounds*, vol. 925, Aug. 2022, Art. no. 166617.

[40] S. C. Ma et al., "Voltage-modulated surface plasmon resonance biosensors integrated with gold nanohole arrays," *Biomed. Opt. Exp.*, vol. 14, no. 1, pp. 182–193, Jan. 2023.

[41] X. Tong et al., "High-sensitivity angle modulation biosensor based on surface plasmon resonance of metasurface," *IEEE Photon. J.*, vol. 14, no. 6, Dec. 2022, Art. no. 5163705.

[42] N. Luan et al., "Orthogonal-sided polished microstructured optical fiber-based SPR sensor for simultaneous measurement of temperature and refractive index," *IEEE Photon. J.*, vol. 14, no. 3, Jun. 2022, Art. no. 6824008.

[43] J. Jing et al., "Performance improvement approaches for optical fiber SPR sensors and their sensing applications," *Photon. Res.*, vol. 10, no. 1, pp. 126–147, Jan. 2022.

[44] Z. Zheng et al., "Terahertz perfect absorber based on flexible active switching of ultra-broadband and ultra-narrowband," *Opt. Exp.*, vol. 29, no. 26, pp. 42787–42799, Dec. 2021.

[45] S. Wang et al., "Gate-tunable plasmons in mixed-dimensional van der Waals heterostructures," *Nature Commun.*, vol. 12, no. 1, pp. 1–8, 2021.

[46] Y. Zhao et al., "Tunable perfect absorption structures based on cavity coupling and plasmon hybrid mode," *IEEE Photon. J.*, vol. 13, no. 2, Apr. 2021, Art. no. 4800109.